Human Molecular Genetics, 2013, Vol. 22, No. 8 **1493–1506**
doi:10.1093/hmg/dds562
Advance Access published on January 7, 2013

The CMT4B disease-causing phosphatases Mtmr2 and Mtmr13 localize to the Schwann cell cytoplasm and endomembrane compartments, where they depend upon each other to achieve wild-type levels of protein expression

Aubree A. Ng[1,†], Anne M. Logan[1,2,†], Eric J. Schmidt[1] and Fred L. Robinson[1,*]

[1]The Jungers Center for Neurosciences Research, Department of Neurology and [2]Neuroscience Graduate Program, Oregon Health & Science University, 3181 SW Sam Jackson Park Road, Portland, OR 97239, USA

Received November 6, 2012; Revised December 17, 2012; Accepted December 27, 2012

The demyelinating peripheral neuropathy Charcot–Marie–Tooth type 4B (CMT4B) is characterized by axonal degeneration and myelin outfoldings. CMT4B results from mutations in either myotubularin-related protein 2 (*MTMR2*; CMT4B1) or *MTMR13* (CMT4B2), phosphoinositide (PI) 3-phosphatases that dephosphorylate phosphatidylinositol 3-phosphate (PtdIns3*P*) and PtdIns(3,5)P_2, lipids which regulate endo-lysosomal membrane traffic. The catalytically active MTMR2 and catalytically inactive MTMR13 physically associate, although the significance of this association is not well understood. Here we show that Mtmr13 loss leads to axonal degeneration in sciatic nerves of older mice. In addition, CMT4B2-like myelin outfoldings are present in *Mtmr13*$^{-/-}$ nerves at postnatal day 3. Thus, *Mtmr13*$^{-/-}$ mice show both the initial dysmyelination and later degenerative pathology of CMT4B2. Given the key role of PI 3-kinase-Akt signaling in myelination, we investigated the state of the pathway in nerves of CMT4B models. We found that Akt activation is unaltered in *Mtmr13*$^{-/-}$ and *Mtmr2*$^{-/-}$ mice. Mtmr2 and Mtmr13 are found within the Schwann cell cytoplasm, where the proteins are partially localized to punctate compartments, suggesting that Mtmr2–Mtmr13 may dephosphorylate their substrates on specific intracellular compartments. Mtmr2–Mtmr13 substrates play essential roles in endo-lysosomal membrane traffic. However, endosomes and lysosomes of *Mtmr13*$^{-/-}$ and *Mtmr2*$^{-/-}$ Schwann cells are morphologically indistinguishable from those of controls, indicating that loss of these proteins does not cause wholesale dysregulation of the endo-lysosomal system. Notably, Mtmr2 and Mtmr13 depend upon each other to achieve wild-type levels of protein expression. Mtmr2 stabilizes Mtmr13 on membranes, indicating that the Mtmr13 pseudophosphatase is regulated by its catalytically active binding partner.

INTRODUCTION

Phosphoinositides (PIs), phosphorylated derivatives of phosphatidylinositol, are found in all eukaryotic organisms (1,2). As membrane-tethered signaling molecules, PIs regulate many processes, including cell division, cell growth and survival, intracellular membrane trafficking, actin dynamics and signaling (1,3). PI kinases, phosphatases and phospholipases collectively regulate PI abundance, turnover and localization, and the importance of this regulation is highlighted by numerous human disease-causing mutations that have been identified in PI kinases and phosphatases (4). However, the cellular mechanisms by which the dysregulation of PIs lead to disease have largely remained unclear.

---

[*]To whom correspondence should be addressed at: The Jungers Center for Neurosciences Research, Department of Neurology, Oregon Health & Science University, Mail Code L623, 3181 SW Sam Jackson Park Road, Portland, OR 97239, USA. Tel: +1 503 494 8783; Fax: +1 503 494 9161; Email: robinsof@ohsu.edu

[†]The authors wish it to be known that, in their opinion, the first two authors should be regarded as joint First Authors.

Mutations in genes encoding proteins involved in PI signaling cause certain forms of Charcot–Marie–Tooth disease (CMT), one of the most common inherited neurological disorders (5). CMT is a heterogeneous collection of peripheral neuropathies that lead to progressive degeneration of the muscles of the extremities and loss of sensory function. Although CMT-causing mutations have been identified in over 40 human genes, the mechanisms by which these mutations lead to disease are generally poorly understood (6–8). CMT type 4B (CMT4B) is a severe, autosomal-recessive form of demyelinating CMT. Nerves from CMT4B patients show severe axonal loss and focally folded myelin sheaths, the latter of which are considered the hallmark of the condition (9). Mutations in myotubularin-related protein 2 (MTMR2) and MTMR13 cause CMT4B1 and CMT4B2, respectively (10–12). MTMR2 and MTMR13 are two members of a large family of PI 3-phosphatases that are key regulators of PIs in eukaryotes (13–16). MTMR2 specifically dephosphorylates phosphatidylinositol 3-phosphate (PtdIns3*P*) and phosphatidylinositol 3,5-bisphosphate (PtdIns [3,5]P_2), two lipids that regulate membrane traffic within the endo-lysosomal pathway (2,17–22). Therefore, it is theorized that CMT4B arises from defects in membrane transport in Schwann cells. Notably, MTMR13 is a catalytically inactive 'pseudophosphatase' that likely functions as a scaffold, binding to MTMR2 and other proteins (23–25).

Mouse models of CMT4B1 and CMT4B2, generated by disrupting *Mtmr2* and *Mtmr13*, recapitulate several key aspects of CMT4B, most notably the striking myelin outfolding (26–29). In addition, Schwann cell-specific deletion of *Mtmr2* is sufficient to cause myelin outfoldings, strongly suggesting that this may be the initially affected cell type in CMT4B1 (30). However, a recent study of *Mtmr2-Fig4* double-knockout mice has uncovered a role for Mtmr2 in neurons as well (31). In this study, we assess whether the axonal degeneration observed in CMT4B2 patients is found in *Mtmr13*$^{-/-}$ mice. Mouse models are proving highly useful for studying the underlying cellular causes of CMT4B. Work with *Mtmr2*$^{-/-}$ mice has led to the proposal of a plausible model in which Mtmr2 functions as part of a regulatory network that titrates membrane addition during myelination (32). However, the specific roles of Mtmr2 and Mtmr13 in the regulation of PdtIns3*P*, PtdIns(3,5)P_2 and endo-lysosomal traffic in Schwann cells remain unclear. Given the enrichment of PdtIns3*P* and PtdIns(3,5)P_2 on endo-lysosomal membranes, the Mtmr2-Mtmr13 complex might be expected to localize to these substrate-rich compartments, but the localization of Mtmr2 and Mtmr13 is unclear.

Here, we have focused on several important questions regarding the cellular etiology of CMT4B. First, where are Mtmr2 and Mtmr13 localized in myelinating Schwann cells? Second, how is the Schwann cell endo-lysosomal pathway impacted by the loss of Mtmr2 or Mtmr13? Third, is the PI 3-kinase-Akt signaling pathway, which is known to promote myelination, dysregulated in mouse models of CMT4B? Finally, we explore the relationship between MTMR2 and MTMR13, focusing on how the two proteins reciprocally regulate protein stability and membrane localization.

RESULTS

Axonal degeneration in the absence of Mtmr13

Symptoms of CMT4B usually appear between the ages of 2 and 13, with muscle atrophy apparent in the distal portions of upper and lower limbs (9). Neurophysiologically, CMT4B is characterized by marked reductions in nerve conduction velocity (NCV), affecting both motor and sensory nerves (9). Nerve biopsies from CMT4B patients show severe axonal loss, with surviving fibers either hypomyelinated or demyelinated. The pathological hallmark of CMT4B is the presence of distinctive myelin outfoldings and infoldings (33,34).

Two mouse models of CMT4B2 have been described, both of which utilize animals with similar gene trap mutations in *Mtmr13* (28,29). *Mtmr13*$^{-/-}$ mice recapitulate several key aspects of human CMT4B2, namely reduced NCV and compound muscle action potential amplitude, as well as myelin outfolding and infolding (28,29). A key component of CMT4B2 is axonal degeneration, which leads to disability in patients (9). However, the extent to which this feature of the condition is recapitulated in *Mtmr13*$^{-/-}$ mice is unclear (28,29). To address this issue, we examined peripheral nerve pathology in 28-month-old *Mtmr13*$^{-/-}$ mice, an advanced age at which we reasoned axonal degeneration might be pronounced. Sciatic nerve cross-sections from *Mtmr13*$^{-/-}$ mice showed a notable decrease in toluidine blue staining, suggesting demyelination or loss of myelinated axons, which was discerned even at low magnification (Fig. 1A and B; Supplementary Material, Table S1). Higher magnification microscopy revealed significant axon loss, evidenced by a statistically significant decrease of nearly 60% in the density of myelinated axons (Fig. 1C–G). In *Mtmr13*$^{-/-}$ nerves, numerous degenerated axon-Schwann cell units were observed, consisting of remnants of Schwann cell membranes and cytoplasm, as well as redundant basal lamina detached from Schwann cells (Fig. 1F). At 28 months, most intact *Mtmr13*$^{-/-}$ axons possessed abnormally folded myelin sheaths (Fig. 1D and F; Supplementary Material, Table S1). Consistent with demyelination and axon loss, we observed reductions in the levels of neurofilament light (NF-L) chain and myelin basic protein (MBP) in aged *Mtmr13*$^{-/-}$ mice (Supplementary Material, Fig. S1).

We also assessed whether older *Mtmr13*$^{-/-}$ mice show hypomyelination, a feature of CMT4B2 that likely reflects suboptimal remyelination following demyelination (9). At 28 months, the surviving *Mtmr13*$^{-/-}$ axons are significantly hypomyelinated, as indicated by a statistically significant increase in the average *g*-ratio, a metric of myelin thickness obtained by dividing the axonal perimeter by the myelin perimeter (Fig. 1H and I; Supplementary Material, Table S1). We observed further evidence of segmental demyelination–remyelination in *Mtmr13*$^{-/-}$ nerves in the presence of 'onion bulb' structures, remnants of Schwann cell membrane and cytoplasm, as well as unattached basal lamina (Fig. 1F, J and K). In summary, peripheral nerves from aged *Mtmr13*$^{-/-}$ mice show clear evidence of axonal degeneration, hypomyelination and segmental demyelination–remyelination, all of which are prominent pathological features of human CMT4B2.

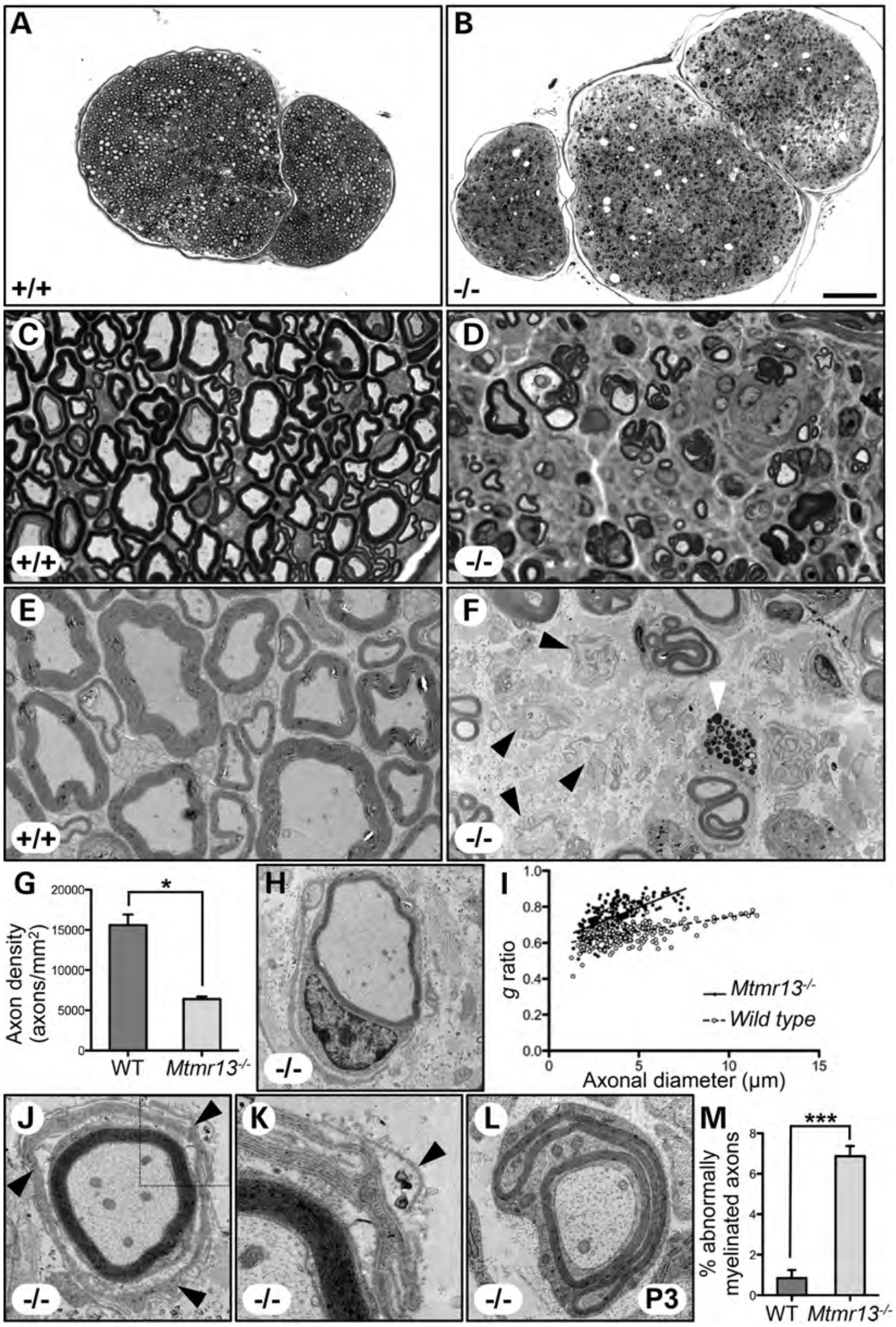

Figure 1. Axonal degeneration, hypomyelination and early dysmyelination in peripheral nerves of *Mtmr13*$^{-/-}$ mice. (**A**–**D**) Light microscopy analysis of sciatic nerves from wild-type and *Mtmr13*$^{-/-}$ mice at 28 months. Toluidine blue-stained cross-sections of the mid-sciatic nerve are shown. *Mtmr13*$^{-/-}$ nerves show a reduction in toluidine blue staining (black), reflecting a significant reduction in the density of myelinated axons, as well as myelin outfolding and infolding (D). (**E** and **F**) EM analysis reveals evidence of axonal degeneration in *Mtmr13*$^{-/-}$ mice, namely remnants of axon-Schwann cell units (arrowheads in F). A mast cell is indicated with a white arrowhead. (**G**) Density of myelinated axons in sciatic nerves of wild-type and *Mtmr13*$^{-/-}$ mice (15 610 ± 1320 myelinated axons/mm^2 for wild-type versus 6402 ± 317.6 for *Mtmr13*$^{-/-}$; $n = 2$ mice for both genotypes; $^{*}P = 0.0211$). (**H**) An example of a hypomyelinated axon in an *Mtmr13*$^{-/-}$ sciatic nerve. (**I**) Myelin thickness (*g*-ratio) in wild-type and *Mtmr13*$^{-/-}$ mice at 28 months (average *g*-ratio: 0.742 ± 0.017 for *Mtmr13*$^{-/-}$ versus 0.654 ± 0.006 for wild-type; $n = 2$; $^{*}P = 0.0395$). (**J**) Examples of supernumerary Schwann cell processes and basal laminae (arrowheads) surrounding a myelinated axon in an *Mtmr13*$^{-/-}$ sciatic nerve. (**K**) A magnification of the indicated portion of (J) in which a detached basal lamina is marked with an arrowhead. (**L**) Myelin outfolding in sciatic nerves of *Mtmr13*$^{-/-}$ mice at P3. (**M**) Frequency of abnormal myelination (outfolding) in P3 wild-type and *Mtmr13*$^{-/-}$ sciatic nerves (0.8456% ± 0.3963 for wild-type versus 6.868% ± 0.5089 for *Mtmr13*$^{-/-}$; $n = 3$ for both; $^{***}P = 0.0007$). Scale bar: 100 µm (A and B), 10 µm (C and D), 4 µm (E and F), 3 µm (H), 1 µm (J), 520 nm (K) and 1 µm (L)

Initial myelination is abnormal in *Mtmr13*$^{-/-}$ mice

In hopes of providing insights into the development of CMT4B2, we sought to determine when myelination first goes awry in the postnatal development of *Mtmr13*$^{-/-}$ mice. To address this issue, we examined *Mtmr13*$^{-/-}$ sciatic nerves at postnatal day 3 (P3), an early stage of myelination when most large axons (>1 μm) are in a 1:1 relationship with Schwann cells and most have acquired a thin myelin sheath. Notably, we found that outfoldings are present to a significant degree in P3 nerves from *Mtmr13*$^{-/-}$ animals, where these structures are about seven times more prevalent than in wild-type nerves (Fig. 1L and M). This finding suggests that initial myelination may be abnormal in CMT4B2. The data we present here indicate that loss of *Mtmr13* in mice recapitulates both the late degenerative pathology and the likely initial myelination abnormalities of CMT4B2, highlighting the utility of this model for the study of the underlying cellular causes of this condition.

Akt activation is unaltered in mouse models of CMT4B

Despite the availability of authentic mouse models of CMT4B, the underlying cellular causes of the condition remain unclear. Although the process of membrane trafficking is implicated, abnormalities in Schwann cell signaling pathways could also cause CMT4B. To address this issue, we investigated the activation of the PI 3-kinase-Akt and extracellular signal-regulated kinase 1/2 (Erk1/2) pathways in sciatic nerves from CMT4B model mice. In addition, we examined the status of Discs-large homolog 1 (Dlg1), a PDZ domain scaffold protein that associates with Mtmr2 (26).

The PI 3-kinase-Akt signaling pathway is a key regulator of cell growth, metabolism and survival, and plays a critical role in myelination. Binding of axonal Nrg1 type III to glial ErbB2/3 receptor tyrosine kinases leads to activation of class I PI 3-kinases, which generate PtdIns(3,4,5)P_3 (3). In Schwann cells and oligodendrocytes, elevated PtdIns(3,4,5)P_3 leads to activation of the Akt kinase pathway, and subsequently mTOR, thus representing a strong pro-myelination signal (35–39). In addition, there is evidence for decreased Akt signaling and/or increased apoptosis in cell culture models where myotubularins have been depleted (15,40–42). Given the potential relevance of Akt signaling to the myotubularin phosphatases and to CMT4B, we examined Akt kinase activation in sciatic nerves of adult *Mtmr13*$^{-/-}$ and *Mtmr2*$^{-/-}$ mice. By monitoring phosphorylation of serine 473, we found that Akt activation was not significantly altered in the absence of Mtmr13 or Mtmr2 (Fig. 2A–C). We also considered the possibility that Akt signaling might be dysregulated during initial myelination in CMT4B model mice but normal in adults. To address this, we examined Akt activation in sciatic nerves from P4 mice. Akt activation was not significantly altered in sciatic nerve extracts from P4 *Mtmr13*$^{-/-}$ or *Mtmr2*$^{-/-}$ mice (Fig. 2F and G).

The Dlg1 scaffold protein regulates polarized membrane addition in *Drosophila* (43,44). Dlg1 binds to Mtmr2, and the localization of Dlg1 to paranodes of Schwann cells is largely eliminated in *Mtmr2*$^{-/-}$ nerves (30). A plausible model has been proposed in which the loss of Dlg1/Mtmr2-mediated control of membrane addition leads to the excessive local myelin deposition observed in CMT4B1 (32). Dlg1 has also been implicated as a negative regulator of Schwann cell myelin thickness via the protein's inhibitory effect on Akt signaling (45). To explore whether Dlg1 function might be altered in *Mtmr13*$^{-/-}$ Schwann cells, we examined the levels of the protein in sciatic nerves. Dlg1 protein levels were not significantly altered in *Mtmr13*$^{-/-}$ sciatic nerves, but were slightly suppressed in *Mtmr2*$^{-/-}$ nerves (Fig. 2A).

Erk1/2 signaling plays an important role in Schwann cell and oligodendrocyte myelination (46,47). Moreover, alterations in PtdIns3*P* levels and endocytosis might be expected to influence growth factor signaling in Schwann cells by controlling the recycling or degradation of activated receptor tyrosine kinases. Accordingly, we examined Erk1/2 activation in peripheral nerves of *Mtmr13*$^{-/-}$ and *Mtmr2*$^{-/-}$ mice. A trend toward higher Erk1/2 activity in the knockout nerves was not statistically significant, suggesting that kinase activation is unaltered in nerves from adult CMT4B model mice (Fig. 2A, D and E). In summary, our investigation of Akt and Erk1/2 activation suggests that alterations in these signaling pathways are not a feature of CMT4B.

Cellular localization of Mtmr2 and Mtmr13 in Schwann cells

A clear understanding of the localization of Mtmr2-Mtmr13 in myelinating Schwann cells will likely be key to determining how membrane traffic and/or signaling are disturbed in CMT4B. However, the subcellular localization of Mtmr2 and Mtmr13, particularly in Schwann cells, is unclear at present. The PI 3–phosphatase complex might be expected to localize to specific endo-lysosomal compartments rich in PtdIns3*P* and/or PtdIns(3,5)P_2, in order to act upon its substrates. Alternatively, Mtmr2–Mtmr13 might be found on membrane compartments lacking PtdIns3*P* and PtdIns(3,5)P_2, thereby acting to prevent the aberrant accumulation of substrates at these locations. In accord with both of these proposals, we and others have used fractionation to demonstrate that significant portions of the endogenous proteins are associated with membranes (23,48).

To investigate the localization of Mtmr2 and Mtmr13, we began by generating affinity-purified rabbit antibodies to both proteins (23). We assessed the specificity of these antibodies by performing immunofluorescence on sciatic nerves from wild-type and mutant mice. Mtmr13 and Mtmr2 immunofluorescence were greatly reduced in *Mtmr13*$^{-/-}$ and *Mtmr2*$^{-/-}$ nerve sections, respectively (Fig. 3A–D), indicating that the antibodies used here are specific for Mtmr13 and Mtmr2. When examined in nerve cross-sections, we observed that both Mtmr13 and Mtmr2 were localized to the Schwann cell and the axoplasm (Fig. 3E and G). Both phosphatases were excluded from the nucleus and from compact myelin (Fig. 3E and G). Within the Schwann cell cytoplasm, both phosphatases were partially localized to punctate structures (Fig. 3E and G). Mtmr13 immunofluorescence was punctate to a greater degree than was Mtmr2 immunofluorescence (Fig. 3E and G). These data strongly suggest that Mtmr13 and

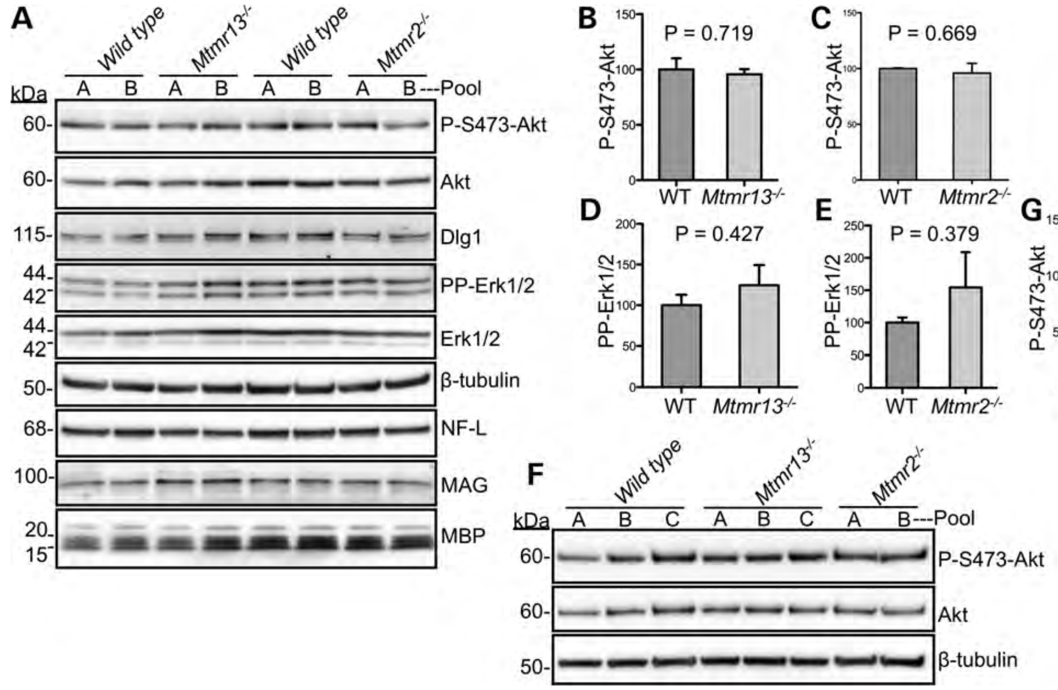

Figure 2. Akt and Erk1/2 activation, and Dlg1 protein levels in mouse models of CMT4B. (**A**) Sciatic nerve extracts were prepared from 4-month-old mice of the indicated genotypes and examined by immunoblotting. Pools A and B denote independent (replicate) pools of nerves of the same genotype. (**B**–**E**) Quantification of protein levels in immunoblots. P-S473-Akt and PP-Erk1/2 values are normalized to the amount of total Akt and total Erk1/2 in each sample. Significant changes in the activation of Akt or Erk1/2 were not observed in *Mtmr13*$^{-/-}$ or *Mtmr2*$^{-/-}$ nerves. (**B**) P-S473-Akt (100.0 ± 10.21 for wild-type versus 95.67 ± 4.676 for *Mtmr13*$^{-/-}$; $n = 3$ for both; $P = 0.7193$). (**C**) *P*-S473-Akt (100.0 ± 0.5739 for wild-type versus 96.00 ± 8.680 for *Mtmr2*$^{-/-}$; $n = 3$ for both; $P = 0.6695$). (**D**) PP-Erk1/2 (100.0 ± 12.96 for wild-type versus 124.7 ± 24.75 for *Mtmr13*$^{-/-}$; $n = 3$ for both; $P = 0.4272$). (**E**) PP-Erk1/2 (100.0 ± 7.745 for wild-type versus for 154.3 ± 54.47 for *Mtmr2*$^{-/-}$; $n = 3$ for both; $P = 0.3792$). The levels of NF-L chain and MBP were not significantly altered in *Mtmr13*$^{-/-}$ of *Mtmr2*$^{-/-}$ nerves. Myelin-associated glycoprotein (MAG) levels were unchanged in *Mtmr2*$^{-/-}$ nerves, but appeared slightly elevated in *Mtmr13*$^{-/-}$ nerves. (**F**) Akt activation in mouse sciatic nerves at P4. (**G**) Quantification of immunoblots in (F). P-S473-Akt values are normalized to the amount of total Akt in each sample. Significant changes in Akt activation were not observed. P-S473-Akt: 100.0 ± 4.615 for wild-type versus 109.1 ± 8.236 for *Mtmr13*$^{-/-}$ versus 119.5 ± 7.147 for *Mtmr2*$^{-/-}$; $n = 3$ for wild-type and *Mtmr13*$^{-/-}$; $n = 2$ for *Mtmr2*$^{-/-}$; $P = 0.3915$ for wild-type versus *Mtmr13*$^{-/-}$ and 0.0920 for wild-type versus *Mtmr2*$^{-/-}$.

Mtmr2 are partially localized to endomembrane compartments in Schwann cells.

Impact of loss of Mtmr2 or Mtmr13 on the Schwann cell endo-lysosomal pathway

There are a number of examples where the loss of the PI kinases or phosphatases that regulate PtdIns3*P* and PtdIns(3,5)P_2 leads to dramatically abnormal endo-lysosomal membranes, usually the swelling or expansion of these compartments (49–54). We therefore evaluated the impact of loss of Mtmr2 or Mtmr13 on the Schwann cell endo-lysosomal pathway. EEA1-positive early endosomes and Lamp1-positive late endosomes/lysosomes in *Mtmr2*$^{-/-}$ and *Mtmr13*$^{-/-}$ myelinating Schwann cells were indistinguishable from those of wild-type controls (Fig. 4A–D). Consistently, endo-lysosomal morphology appeared normal in primary *Mtmr2*$^{-/-}$ and *Mtmr13*$^{-/-}$ Schwann cells (Fig. 4E–H) and in mouse embryo fibroblasts (MEFs) derived from mutant embryos (Supplementary Material, Fig. S2). We also examined lysosome morphology in Schwann cells, using high-magnification EM. Lysosome size was not significantly altered in myelinating Schwann cells of *Mtmr13*$^{-/-}$ nerves (Supplementary Material, Fig. S4). In accord with our morphological findings, Lamp1 protein levels were unaltered in sciatic nerves, brains and MEF cells from *Mtmr13*$^{-/-}$ and *Mtmr2*$^{-/-}$ mice (Fig. 4I and J; Supplementary Material, Fig. S2). During our ultrastructural (EM) analysis of lysosomes (Supplementary Material, Fig. S4), abnormalities were not apparent in other organelles or vesicular populations (data not shown). Clathrin-coated pits were identified in both wild-type and *Mtmr13*$^{-/-}$ Schwann cells, although a quantitative evaluation of the prevalence of these structures was not possible.

To investigate a potentially relevant effector of PtdIns3*P*, we sought to evaluate the function of the retromer complex in Schwann cells of CMT4B model mice. The retromer complex, composed of sorting nexins 1 and 2 (Snx1/2), Vps26, Vps29 and Vps35, acts to recycle the cation-independent mannose 6-phosphate receptor (CI-MPR) from late endosomes to the trans-Golgi network in a PtdIns3*P*-dependent manner. Consistently, perturbations affecting PtdIns3*P* levels have been shown to alter the localization and/or abundance of Snx1/2, Vps26 and CI-MPR or its yeast homolog Vps10p (55,56). Although we were unable to identify antibodies suitable for assessing the localization or abundance of CI-MPR in Schwann cells, we examined the levels of several components of retromer in sciatic nerve or brain extracts. We found that the levels of Snx1 and Vps26 in *Mtmr13*$^{-/-}$ and *Mtmr2*$^{-/-}$

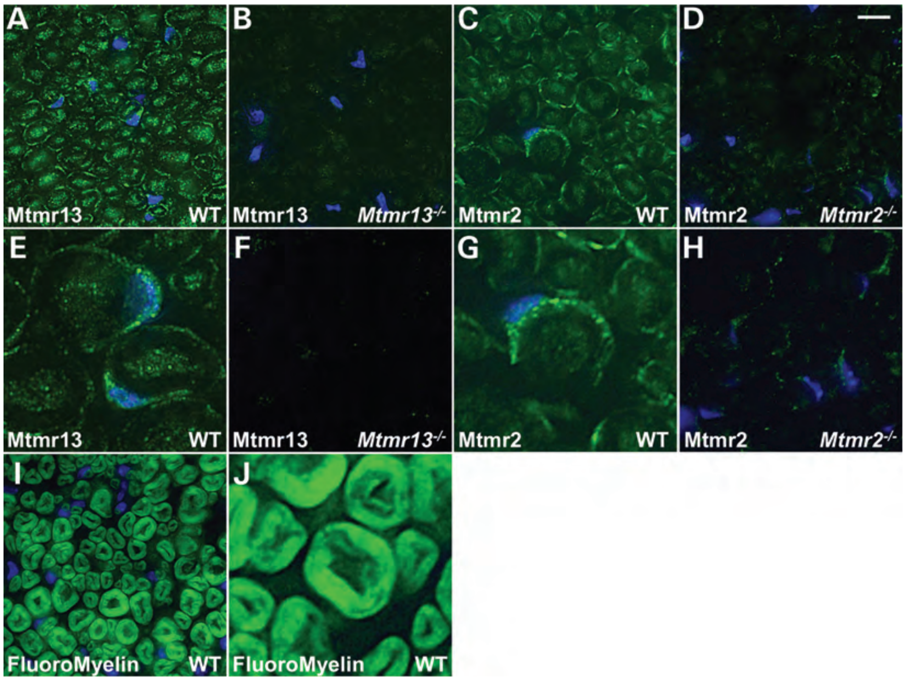

Figure 3. Specificity of anti-Mtmr13 and anti-Mtmr2 antibodies and localization within Schwann cells and axons. Cross-sections of sciatic nerves from 8- or 9-month-old mice were examined by immunofluorescence microscopy. (**A**) Anti-Mtmr13 immunofluorescence (green) is greatly reduced in sciatic nerve sections from *Mtmr13*$^{-/-}$ mice (**B**). (**C**) Anti-Mtmr2 immunofluorescence (green) is greatly reduced in sciatic nerve sections from *Mtmr2*$^{-/-}$ mice (**D**). (A)–(D) depict representative data from one of four independent experiments. (**E**) Localization of Mtmr13 in wild-type mouse sciatic nerves. Anti-Mtmr13 immunofluorescence (green) is detected in the Schwann cell cytoplasm and the axon, but is excluded from compact myelin and the Schwann cell nucleus. Punctate Mtmr13-positive structures are detected in the Schwann cell cytoplasm. (**F**) Anti-Mtmr13 immunofluorescence (green) is greatly reduced in an *Mtmr13*$^{-/-}$ nerve section comparable with (E) under identical acquisition settings. (**G**) Localization of Mtmr2 in wild-type mouse sciatic nerves. Anti-Mtmr2 immunofluorescence (green) is detected in the Schwann cell cytoplasm and the axon, but is excluded from compact myelin and the Schwann cell nucleus. Punctate Mtmr2-positive structures are detected in the Schwann cell cytoplasm. (**H**) Anti-Mtmr2 immunofluorescence (green) is greatly reduced in an *Mtmr2*$^{-/-}$ nerve section comparable with (G) under identical acquisition settings. (**I** and **J**) FluoroMyelin staining identifies compact myelin in sections comparable with those of (A)–(D) and (E)–(H), respectively. Nuclei were labeled with DAPI (blue). Scale bar: 10 μm (A–D and I), 4 μm (E–H and J).

nerves were similar to controls (Fig. 4I, K and L). Likewise, Vps26 and Vps35 levels were normal in brain extracts from mutant mice (Supplementary Material, Fig. S2F, H and I). A definitive assessment of retromer function in mouse models of CMT4B will require further studies focused on the status the retromer cargo CI-MPR.

Mtmr2 and Mtmr13 depend upon each other to achieve wild-type levels of protein expression in peripheral nerves

We have demonstrated that Mtmr2 and Mtmr13 physically interact (23), a finding subsequently supported by others (24). However, the biological function of Mtmr2–Mtmr13 association remains enigmatic. To further explore the relationship between the proteins, we examined the levels of each in sciatic nerves of mutant mice. We consistently observed a 50% reduction in Mtmr2 protein levels in *Mtmr13*$^{-/-}$ nerves (Fig. 5A and B). Likewise, Mtmr13 protein levels were reduced by ~70% in *Mtmr2*$^{-/-}$ nerves (Fig. 5A and C). To investigate whether Mtmr2 and Mtmr13 enhance each protein's abundance in other tissues and in primary fibroblasts, we evaluated the levels of the two proteins in brain extracts and MEFs. Loss of Mtmr2 or Mtmr13 does not alter the levels of the binding partner in brain extracts or MEF cells (Fig. 5D and E). Thus, in a CMT4B-relevant tissue, loss of either Mtmr2 or Mtmr13 lowers the abundance of the other protein by 50 or 70%, respectively.

To further explore what appears to be a novel, stabilizing effect of Mtmr2 upon Mtmr13, we investigated the membrane association of the two proteins. MTMR2 and MTMR13 were expressed in HEK293 cells and membrane and cytosolic fractions were isolated (Fig. 6). MTMR2 was present in both membrane and cytosolic fractions; MTMR13 was predominantly found in the membrane fraction, and was not detected in the cytosol (Fig. 6B). Notably, the co-expression of MTMR2 substantially enhanced the abundance of MTMR13 in the membrane fraction (Fig. 6B).

To assess whether the stabilizing effect of MTMR2 on membrane-associated MTMR13 requires direct association, we tested whether deletion of coiled-coil sequences would decrease the abundance of MTMR13. Indeed, a mutant form of MTMR2 lacking the coiled-coil sequence (MTMR2-ΔCC) failed to enhance MTMR13 levels in the membrane fraction (Fig. 6B). Consistently, the abundance of MTMR13-ΔCC, which is incapable of association with MTMR2, was not enhanced by the expression of MTMR2 (Fig. 6B). The abundance of another mutant, MTMR13-ΔPH, which lacks the C-terminal PH domain and the PDZ domain-binding motif, but retains the coiled-coil motif, was enhanced by the co-expression of MTMR2 (Fig. 6B). In summary, the

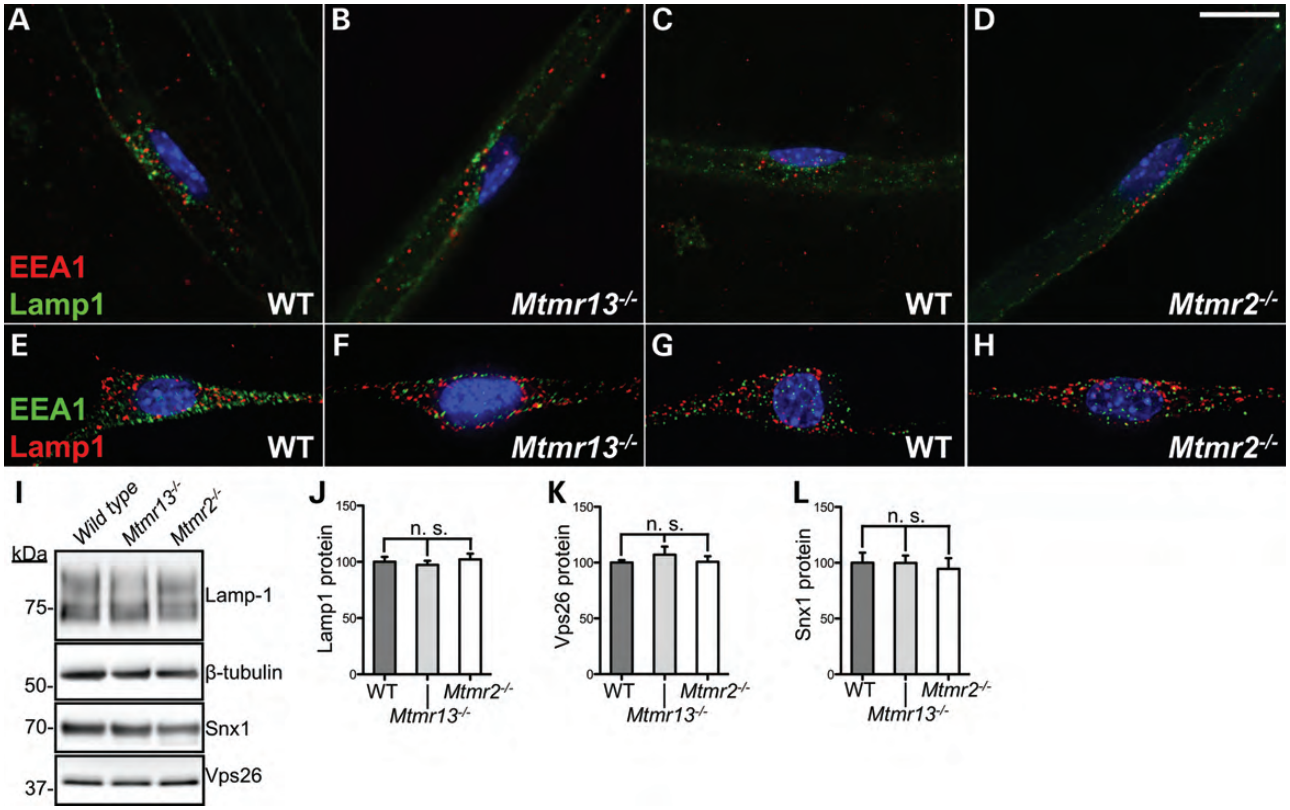

Figure 4. Status of endo-lysosomal membranes in CMT4B model Schwann cells and sciatic nerves. (**A**–**D**) Immunofluorescence was performed on teased myelinated fibers from sciatic nerves of wild-type, *Mtmr13*$^{-/-}$ and *Mtmr2*$^{-/-}$ mice aged 110 days (A and B) or 58 days (C and D). Lamp1-positive late endosomes/lysosomes (green) and EEA1-positive early endosomes (red) in *Mtmr2*$^{-/-}$ and *Mtmr13*$^{-/-}$ Schwann cells appear similar to wild-type, without evidence of endo-lysosomal swelling. (**E**–**H**) Immunofluorescence was performed on primary Schwann cells of the indicated genotypes. Lamp1-positive late endosomes/lysosomes (red) and EEA1-positive early endosomes (green) in *Mtmr2*$^{-/-}$ and *Mtmr13*$^{-/-}$ Schwann cells appear similar to wild-type. Nuclei were stained with DAPI (blue). Scale bar: 15 μm (A–D), 17 μm (E and F) and 13 μm (G and H). (**I**) Sciatic nerve protein extracts were prepared from 4-month-old mice of the indicated genotypes and examined by immunoblotting. (**J**–**L**) Quantification of immunoblots in (I). Lamp1, Vps26 and Snx1 values are normalized to the amount of β-tubulin in each sample. Significant changes in Lamp1, Vps26 and Snx1 levels were not observed. Lamp1 protein levels: 100.0 ± 4.496 for wild-type versus 97.35 ± 3.613 for *Mtmr13*$^{-/-}$ versus 102.2 ± 5.057 for *Mtmr2*$^{-/-}$; $n = 3$ for all genotypes; $P = 0.6693$ for wild-type versus *Mtmr13*$^{-/-}$; $P = 0.7566$ for wild-type versus *Mtmr2*$^{-/-}$. Vps26 protein levels: 100.0 ± 2.160 for wild-type versus 107.1 ± 7.155 for *Mtmr13*$^{-/-}$ versus 100.7 ± 4.995 for *Mtmr2*$^{-/-}$; $n = 2$ for all genotypes; $P = 0.4416$ for wild-type versus *Mtmr13*$^{-/-}$; $P = 0.9152$ for wild-type versus *Mtmr2*$^{-/-}$. Snx1 protein levels: 100.0 ± 9.064 for wild-type versus 99.81 ± 6.647 for *Mtmr13*$^{-/-}$ versus 94.60 ± 9.641 for *Mtmr2*$^{-/-}$; $P = 0.9870$ for wild-type versus *Mtmr13*$^{-/-}$; $P = 0.7042$ for wild-type versus *Mtmr2*$^{-/-}$; $n = 3$ for all genotypes.

enhanced abundance of membrane-associated MTMR13 requires direct association with MTMR2.

DISCUSSION

Mtmr13-deficient mice model both the initial dysmyelination and advanced degenerative pathology of CMT4B2

Mtmr13$^{-/-}$ mice show myelin outfoldings and deficits in electrophysiology, both consistent with CMT4B2 (28,29). However, the clinically critical aspect of CMT4B2 is axonal loss, as the degree of axonal degeneration is considered the best correlate of clinical deterioration in patients with demyelinating CMT (57). Although examples of axonal degeneration were reported in *Mtmr13*$^{-/-}$ mice at about 14 months of age, the dramatic fiber loss observed in CMT4B2 patients was not evident, and a quantitative assessment of axonal degeneration in these mice is lacking (28,29). To address this issue, we examined the mid-sciatic nerves of mice at 28 months, when we reasoned axonal degeneration might be more pronounced. In these older animals, we found significant axon loss, with the density of myelinated axons reduced by nearly 60%. The axon density we report for nerves of 28-month-old *Mtmr13*$^{-/-}$ mice (6402 myelinated axons/mm^2) is broadly similar to that reported for sural nerves of 2- and 3-year-old CMT4B patients (8400 myelinated axons/mm^2) (34).

In a second aspect of this study, we determined that CMT4B2-like myelin outfoldings arise during initial myelination, as these features are present in the sciatic nerves of P3 *Mtmr13*$^{-/-}$ mice. Thus, loss of Mtmr13 may cause a defect in initial myelination rather than, or in addition to, abnormalities in myelin remodeling or sheet homeostasis, as suggested for Mtmr2 (26,31). We conclude that *Mtmr13*$^{-/-}$ mice are an effective model of both the likely initial dysmyelination and the advanced axonal pathology of CMT4B2, highlighting the strength of this model for investigation of the underlying cellular causes of CMT4B2.

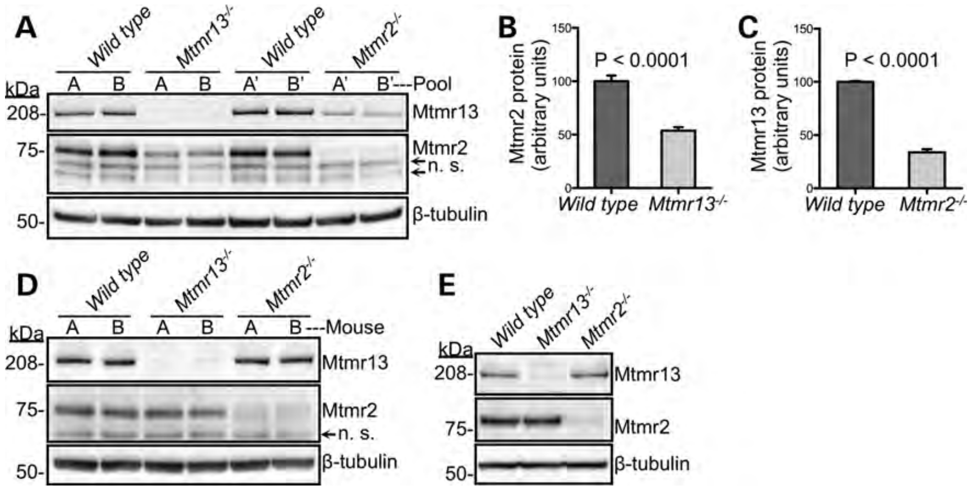

Figure 5. Reciprocal enhancement of protein abundance by Mtmr13 and Mtmr2 in mouse sciatic nerves. (**A**) Sciatic nerve protein extracts were prepared from 4-month-old mice of the indicated genotypes and examined by immunoblotting. Pools A and B denote independent (replicate) pools of nerves of the same genotype. Non-specific (n. s.) bands are indicated in the MTMR2 blots. (**B** and **C**) Chemiluminescent quantification of protein levels in immunoblots. (B) Mtmr2 protein levels: 100.0 ± 5.493 for wild-type versus 53.73 ± 3.371 for *Mtmr13*$^{-/-}$; $n = 5$ for both; $P < 0.0001$. (C) Mtmr13 protein levels: 100.0 ± 0.7643 for wild-type versus 33.87 ± 2.942 for *Mtmr2*$^{-/-}$; $n = 5$ for both; $P < 0.0001$. (**D**) Mtmr13 and Mtmr2 proteins levels in brain extracts from 4-month-old mice were examined by immunoblotting. Mtmr13 levels in the brain: 100.0 ± 9.348 for wild-type versus 100.0 ± 7.331 for *Mtmr2*$^{-/-}$; $n = 4$ for both; $P = 1.0000$. Mtmr2 levels in the brain: 100.0 ± 1.224 for wild-type versus 100.0 ± 5.254 for *Mtmr13*$^{-/-}$; $n = 4$ for both; $P = 1.0000$. (**E**) Protein extracts from MEF cells were examined by immunoblotting.

Akt activation is unaltered in mouse models of CMT4B1 and CMT4B2

The PI 3-kinase/Akt signaling pathway plays a critical role in promoting myelination (35–39). Given the potential relevance of Akt signaling to the pathology of CMT4B, we examined activation of the kinase in sciatic nerves of *Mtmr2*$^{-/-}$ and *Mtmr13*$^{-/-}$ mice, both during initial myelination (day 4) and in adults (3–4 months). We found no significant change in the degree of Akt activation in these models of CMT4B.

A recent study demonstrated that the loss of Pten in Schwann cells causes myelin outfoldings similar to those observed in CMT4B (58). Myelin outfoldings and tomacula in *Pten*$^{-/-}$ nerves very likely result from elevated PtdIns(3,4,5)P_3 levels and elevated Akt signaling. The authors suggest that myelin outfoldings and tomacula may represent a 'final common pathway' or phenotype, which can be triggered by mutations in a number of proteins with very different functions (58), although involvement in PI signaling appears to be a recurring theme (8,59). Our data on Akt activation in CMT4B model nerves are consistent with this model, as while the authors observed a dramatic enhancement of Akt phosphorylation in *Pten*$^{-/-}$ nerves, we report here that Akt phosphorylation in *Mtmr2*$^{-/-}$ and *Mtmr13*$^{-/-}$ nerves is normal (58). Thus, in the models of CMT4B that we have analyzed, myelin outfoldings do not correlate with elevated Akt phosphorylation.

The results of our investigation of Akt signaling might be viewed as in conflict with another study in which investigators compared Akt activation in sciatic nerves of wild-type and *Mtmr2*$^{-/-}$*Mtmr13*$^{-/-}$ double-knockout mice (60). The authors concluded that Akt phosphorylation was impaired in *Mtmr2*$^{-/-}$*Mtmr13*$^{-/-}$ double knockout nerves, but that these nerves contained higher levels of total Akt, apparently having compensated to maintain a wild-type level of phospho-Akt. Our results cannot be compared directly with those of this report (60) due to differences in the genotypes of the mice examined (*Mtmr2*$^{-/-}$*Mtmr13*$^{-/-}$ mice in our study versus double knockout mice in the earlier study) (60).

Mtmr2 and Mtmr13 partially localize to Schwann cell endomembrane compartments

The substrates of Mtmr2–Mtmr13, PtdIns3P and PtdIns(3,5)P_2, play key functions in endo-lysosomal membrane trafficking (2,20–22). Accordingly, PtdIns3P is most highly enriched on early endosomes and on the internalized vesicles of multivesicular endosomes (61). The localization of PtdIns(3,5)P_2 is less well understood, but experiments indicate roles for this lipid in endo-lysosomal membrane trafficking, notably in endosome to *trans*-Golgi network traffic (21,22,62,63).

When over-expressed in mammalian cell lines, MTMR2 exhibits a predominantly cytoplasmic localization (17,23,24,64). In nerves, endogenous Mtmr2 was found to be present in both Schwann cells and neurons/axons (65). Within myelinating Schwann cells, Mtmr2 was detected in all cytoplasmic compartments, including the paranode, and was excluded from the compact myelin (65). The subcellular localization of MTMR13 is particularly poorly understood, with diffuse cytoplasmic localization reported in cell lines overexpressing the protein (23,24,66).

Our understanding of the functions of Mtmr2 and Mtmr13 in Schwann cells has been hampered by a lack of knowledge of the subcellular localization of the complex. To address this issue, we prepared rabbit antibodies to both Mtmr2 and Mtmr13 and demonstrated that these antibodies are specific for the endogenous mouse proteins. We then demonstrated that both Mtmr2 and Mtmr13 localize to the Schwann cell cytoplasm and to punctate, presumably endomembrane, structures within the cytoplasm. Mtmr2 and Mtmr13 are excluded

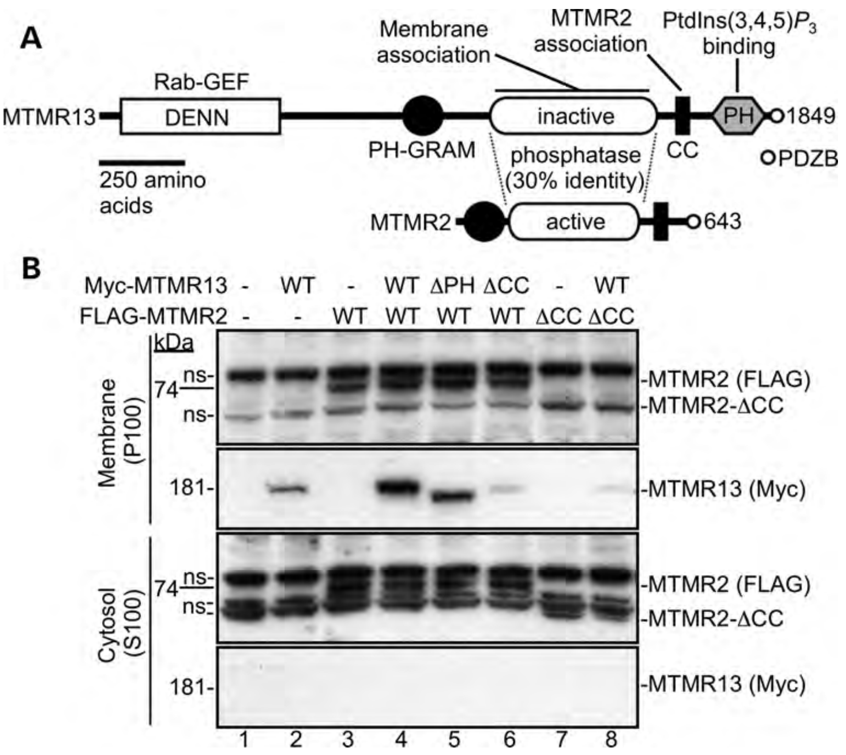

Figure 6. Mtmr13 is stabilized on membranes by Mtmr2. (**A**) A schematic of the composition of the MTMR13 and MTMR2 proteins, indicating functions attributed to specific domains of MTMR13. (**B**) Subcellular fractionation of MTMR13 and MTMR2 following exogenous expression in HEK293 cells. Transfected cells were fractionated into membrane (P100) and cytosolic (S100) fractions and examined by immunoblotting. The anti-FLAG antibody recognizes several nonspecific (ns) proteins that are present in both the P100 and S100 fractions. PH, pleckstrin homology; DENN, differentially expressed in neoplastic versus normal cells; GRAM, glucosyltransferase Rab activator myotubularins; PDZB, PDZ domain-binding motif; GEF, guanine nucleotide exchange factor; CC, coiled-coil.

from the compact myelin and the nucleus. Our data represent the first report on the localization of the endogenous Mtmr13 protein. The localization we report here for Mtmr2 is consistent with a previous study's conclusion that endogenous Mtmr2 localizes to the Schwann cell cytoplasm (65), although the punctate nature of Mtmr2 localization has not been reported previously.

Although we have demonstrated that Mtmr2 and Mtmr13 partially localize to endomembrane compartments in the cytoplasm of myelinating Schwann cells, the identity of such structures remains unclear. We have attempted to determine whether the Mtmr2- and Mtmr13-positive compartments are early endosomes, late endosomes/lysosomes or recycling endosomes, using antibodies to EEA1, Lamp1 and Rab11, respectively. However, such studies have been hampered by the poor performance of our rabbit Mtmr2 and Mtmr13 antibodies in teased fibers, possibly due to cross-reactions with other myotubularin family members such as Mtm1, Mtmr1 and Mtmr5 (26,30). In addition, difficulties in using mouse or rat Lamp1, EEA1 and Rab11 antibodies in frozen sciatic nerve cross-sections have prevented effective co-labeling with our rabbit Mtmr2/13 antibodies in this preparation, highlighting the difficulties of determining the endogenous localizations of myotubularin phosphatases (13,26).

A recent study has provided significant insights into the functions of the *Drosophila* orthologs of mammalian MTMR2/MTM1/MTMR1 (Mtm in flies) and MTMR13/MTMR5 (Sbf in flies) (25). Sbf was found to coordinate both PtdIns3*P* turnover and Rab21 activation in a pathway that regulates endosomal trafficking and cell shape change in fly macrophages. Sbf scaffolds a complex (containing Pi3K68D and Mtm) that promotes endosomal PtdIns3*P* turnover and membrane efflux to a Rab11-mediated recycling pathway that is essential for plasma membrane protrusions (25). Future studies might be aimed at determining whether MTMR2 and MTMR13 perform analogous functions in Schwann cells, and also at assessing the role of phosphorylation in the regulation of MTMR2 localization (67).

Status of the endo-lysosomal pathway in the absence of Mtmr2 or Mtmr13

A number of studies have documented dramatic swelling of endo-lysosomal compartments when the relevant PI kinases or phosphatases are lost or inhibited (49–54). In contrast, we found that the morphology of EEA1- and Lamp1-positive compartments appeared normal in $Mtmr13^{-/-}$ and $Mtmr2^{-/-}$ Schwann cells and fibroblasts. Our result stands in stark contrast to the dramatic upregulation of late endosomal/lysosomal membranes observed in fibroblasts and neurons that lack the PtdIns(3,5)P_2 5-phosphatase Fig4 (31,52). In summary, our findings suggest that loss of either Mtmr2 or Mtmr13 does not cause wholesale dysregulation of the endo-lysosomal membrane system in Schwann cells. Future studies will examine PtdIns3P and PtdIns(3,5)P_2 levels in mouse models of CMT4B2 and determine the impact of loss of Mtmr2 and Mtmr13 on the trafficking of specific cargo proteins.

Mtmr2 and Mtmr13 reciprocally enhance each protein's abundance in peripheral nerves

Mutations in either *MTMR2* or *MTMR13* cause very similar forms of the pathologically distinctive CMT4B, suggesting that the two proteins share similar functions (10–12). We have demonstrated that MTMR2 and MTMR13 physically associate (23). An *in vitro* enzymatic analysis suggested that the Mtmr2–Mtmr13 complex possesses a higher specific activity for PtdIns3P and PtdIns(3,5)P_2 than does Mtmr2 (24). However, the biological significance of Mtmr2–Mtmr13 association, particularly in cell types relevant to CMT4B, remains unclear.

Here, we have examined the Mtmr2–Mtmr13 protein relationship by focusing on protein stability and membrane association. We find that loss of either Mtmr2 or Mtmr13 decreases the other protein's abundance in sciatic nerves. Notably, in both the brain and MEF cells, loss of either Mtmr2 or Mtmr13 has no impact on the abundance of the other. Thus, the mutual dependence of the two proteins appears to be specific for peripheral nerves, suggesting that it may be relevant to CMT4B disease. While we previously observed reduced Mtmr2 levels in nerve extracts from *Mtmr13*$^{-/-}$ mice, our initial study was performed using immunoprecipitation (29). Here, we employ the more definitive approach of directly immunoblotting protein extracts. As an inactive phosphatase and likely scaffold protein (25), MTMR13 might have been viewed as a regulatory subunit of MTMR2. In contrast, our results indicate that Mtmr13 is even more dependent on Mtmr2 for its wild-type level of protein abundance than the reverse. This raises the possibility that some aspects of CMT4B1 (MTMR2 deficiency) might result from decreased MTMR13 function, although we emphasize that our results were obtained in mouse models and cultured cells. In the absence of MTMR2, perhaps some MTMR13-specfic functions are impaired, such as the Rab-GEF activity of the DENN domain (25,68).

The regulation of membrane association is likely an important mechanism by which the function of MTMR2–MTMR13 is controlled, as this property dictates access to substrates. We have demonstrated that significant fractions of the endogenous MTMR2 and MTMR13 proteins are associated with membranes in cultured cell lines, that the pseudophosphatase domain of MTMR13 is sufficient for membrane association and that the two proteins associate in a manner that requires coiled-coil motifs (23). Here, we show that physical association with MTMR2 substantially enhances the abundance of MTMR13 on membranes in HEK293 cells. MTMR2 likely retargets MTMR13 from the cytosol to membranes, simultaneously stabilizing the pseudophosphatase. These findings may be relevant to sciatic nerves, as we consistently observe a 70% reduction in Mtmr13 levels in *Mtmr2*$^{-/-}$ extracts from this tissue. A recent study in *Drosophila* demonstrated that Sbf acts to recruit Mtm into stable complexes on vesicular and cortical membranes of fly cells (25). Our data suggest an analogous, but reversed situation in mammalian cells, with MTMR2 acting to recruit MTMR13 to membranes while simultaneously stabilizing the pseudophosphatase.

The nature of the membrane trafficking events regulated by Mtmr2 and Mtmr13 in Schwann cells remains largely unknown. We have demonstrated that, at least at a morphological level, Schwann cell early endosomes and late/endolysosomes are not significantly altered by the loss of Mtmr2 or Mtmr13, indicating a more subtle disruption of traffic than that observed in cells lacking Fig4 (31,52). Future studies will focus on the identification of specific membrane proteins that may be abnormally trafficked in the absence of Mtmr2 or Mtmr13, as well as on defining how PtdIns3P and PtdIns(3,5)P_2 are dysregulated by the loss of these proteins.

MATERIALS AND METHODS

Antibodies

The anti-MTMR13 antibody (116-AN) was generated by immunizing rabbits with a recombinant protein consisting of the C-terminal PH domain from human MTMR13. The anti-MTMR2 antibody (119-AN) was generated by immunizing rabbits with full-length, recombinant, human MTMR2 containing an N-terminal His$_6$ tag. Anti-MTMR2 (119-AN) and anti-MTMR13 (116-AN) antibodies were affinity-purified from the serum of rabbits 119 and 116, respectively, using columns of His$_6$-MTMR2 and PH-MTMR13 proteins, respectively. Rabbit anti-Akt, anti-phospho-Akt (Ser473), anti-ERK1/2 and anti-EEA1 were obtained from Cell Signaling Technology. Rat anti-LAMP-1 (1D4B) and mouse anti-β-tubulin (E7) were obtained from the Developmental Studies Hybridoma Bank. Mouse anti-SAP97 (Dlg1) (K64/15) was obtained from the UC Davis/NIH NeuroMab Facility. Rabbit anti-MAG was from Santa Cruz Biotechnology. Rabbit anti-VPS26, anti-VPS35 and anti-SNX1 antibody were from Abcam. Rabbit anti-NF-L and rat anti-MBP were obtained from Millipore. Mouse anti-FLAG (M2) and anti-c-myc (9E10) were from Sigma–Aldrich and Roche Applied Science, respectively. Rabbit anti-PP-ERK1/2 (pT185-pY187) was from Invitrogen. Mouse anti-S100β was obtained from BD Biosciences.

Protein analysis

Sciatic nerves (from sciatic notch to knee) were dissected and frozen using liquid nitrogen. Mice were mostly males and were between 2 and 6 months of age (average age for all mice was 3.9 months). Each nerve extract resulted from the pooling and homogenizing of four or six sciatic nerves, with six nerves being more common. Each P4 nerve extract was generated by pooling six nerves. Nerves were pooled according to genotype and homogenized in ice-cold lysis buffer [120 mM NaCl/50 mM Tris, pH 8.0/0.5% Triton X-100/100 mM sodium fluoride/1 mM sodium orthovanadate, 2 mM sodium EDTA, supplemented with cOmplete, EDTA-free Protease Inhibitor Cocktail Tablets (Roche Applied Science) at a concentration of one tablet per 10 ml of buffer]. Brain protein extracts were prepared by homogenizing freshly dissected brains in ice-cold lysis buffer. Monolayers of MEF cells were washed once with PBS and directly lysed in lysis buffer. Homogenates were cleared by centrifugation (17 000g for 15 min at 4°C). Protein concentration was determined and lysates were suspended in NuPAGE LDS sample buffer (Invitrogen) containing 1 mM DTT. Protein extracts (17, 20, 17.5 and 7 μg per lane for sciatic nerves, brains, MEFs and P4 nerves, respectively) were resolved in 4–12% NuPAGE Bis–Tris gels (Invitrogen) in MOPS buffer, transferred to polyvinylidene difluoride membranes, and analyzed by immunoblotting. SuperSignal West Chemiluminescent Substrate (Thermo Scientific) was used for detection, and quantitation was with a G:BOX Chemi imaging system using the GeneSys software (Syngene). Protein levels are presented in arbitrary units with wild-type set to 100, and data as mean ± standard error of the mean. Statistical significance was evaluated using unpaired *t*-tests.

Cell culture and transfection

Primary MEFs were cultured in Dulbecco's modified Eagle's medium (DMEM) (high glucose) supplemented with 10% fetal bovine serum (FBS) and 1% penicillin/streptomycin at 37°C, 5% CO_2. Cells were passaged no more than seven times. HEK293 cells were cultured and transfected as previously described (23). Primary mouse Schwann cells were prepared from single mouse embryos (P13.5) by a previously described method (69). For routine culture, Schwann cells were maintained in Schwann cell growth medium [DMEM with 10% FBS supplemented with 10 ng/ml neuregulin (R & D Systems) and 5 μl/ml forskolin (Sigma–Aldrich)] at 37°C, 10% CO_2 and passaged no more than four times. Bright-field images were taken on an AMG EVOS transmitted light microscope with a CaChN 10×/0.25 PhP objective.

Immunofluorescence

For cryosections, sciatic nerves were dissected and fixed in 4% paraformaldehyde (PFA)/4% sucrose in PBS on ice for 30 min, cryoprotected in 30% sucrose, embedded in OCT and snap-frozen in a dry ice/isopentane bath. Alternatively, mice were perfused with 4% PFA in PBS prior to nerve dissection, with nerves subsequently processed as described above. Nerves were cryosectioned into 8 μm transverse sections, mounted on glass slides and stored at −20°C. Cryosections were washed once in PBS, permeabilized in 0.2% Triton X-100 in PBS for 15 min and blocked with 0.5% fish skin gelatin (Sigma–Aldrich). Anti-MTMR2 and anti-MTMR13 primary antibodies were prepared in 0.05% fish skin gelatin at 1:1000 and incubated for 18 h at 4°C. Cryosections were washed in PBST and incubated with rabbit Alexa 488-conjugated secondary antibody at 1:500 for 1 h. For fluorescent myelin staining, cryosections were permeabilized as described earlier and incubated for 20 min in PBS containing FluoroMyelin^{TM} (Molecular Probes) at a 1:300 dilution.

For teased fiber immunofluorescence, sciatic nerves were dissected, fixed in 4% PFA on ice for 30 min and washed three times in PBS. To tease individual fibers, the perineurium was removed and segments were subdivided on microscope slides using fine forceps. Slides were dried at room temperature for 18 h and stored at −20°C. Slides were washed once in PBS, permeabilized as described earlier and blocked with 0.5% fish skin gelatin (Sigma–Aldrich). Slides were incubated with primary antibodies prepared in 0.05% fish skin gelatin for 18 h at 4°C, washed with PBST and incubated with Alexa 488- or Cy3-conjugated secondary antibodies at 1:500 for 1 h. MEF cells were plated on poly-D-lysine coated cover slips at 75% confluency. Cover slips were washed in PBS and cells were fixed in 4% PFA in PBS for 15 min. Cover slips were then washed three times in PBS, permeabilized as described earlier and blocked with 10% normal goat serum (NGS; Jackson ImmunoResearch). Cover slips were incubated with primary antibodies prepared in 2% NGS for 18 h at 4°C, washed with PBST and incubated with Alexa 488- or Cy3-conjugated secondary antibodies at 1:500 for 1 h. After secondary antibody treatment, cover slips or slides were washed with PBST, stained with DAPI (Molecular Probes) and mounted in Elvanol mounting medium. Schwann cells were plated on poly-L-lysine-coated cover slips at 75% confluency. Cover slips were fixed and permeablized as described earlier and blocked with 0.5% fish skin gelatin (Sigma–Aldrich). Cover slips were incubated with primary antibodies prepared in 0.05% fish skin gelatin for 18 h at 4°C, washed with PBST and incubated with Alexa 488- or Cy3-conjugated secondary antibodies at 1:500 for 1 h. After secondary antibody treatment, cover slips or slides were washed with PBST, stained with DAPI (Molecular Probes) and mounted in Elvanol mounting medium.

The images were acquired on a wide-field DeltaVison CoreDV deconvolution microscopy system (Applied Precision), built on an Olympus IX71 inverted microscope equipped with a Nikon Coolsnap ES2 HQ camera. Each image was acquired as a set of Z-stacks in a 1024 × 1024 format with a 60× 1.42 NA PlanApo objective using Cy3 and/or Alexa488 fluors. The pixel size was 0.107 × 0.107 × 0.2 μm^3. The images were deconvolved with the appropriate optical transfer function using an iterative algorithm of 10 iterations. The histogram was optimized for the brightest image and applied to all the other images for consistency before projection images were made from the Z-stack by merging into a 24-bit TIFF file. The number of Z-sections compressed in each image was the same for comparable images. Acquisition and deconvolution were accomplished using the softWoRx software (Applied Precision). Post-acquisition imaging was accomplished using the Volocity software (Perkin Elmer).

Fractionation

A 150 mm dish of HEK293 cells was transfected with FLAG-MTMR2, FLAG-MTMR2-ΔCC (Δcoiled-coil; Δ589–643), Myc-MTMR13, Myc-MTMR13-Δ1630–1682 (Δcoiled-coil, ΔCC) or Myc-MTMR13-Δ1683-1849 (ΔPH) as previously described (23). Monolayers of cells were washed once with PBS and collected in 10 ml of PBS. Cells were pelleted by centrifugation (1000*g* for 5 min at 4°C), resuspended in 3 ml of ice-cold hypotonic lysis buffer [10 mM Tris (pH 7.5), 1 mM NaF, 10 mM NaCl, 1 mM Na_2VO_4, 1 μg/ml Leupeptin, 10.5 μg/ml aprotinin, 1 μg/ml pepstatin, 1 mM PMSF, 1 mM benzamidine, 1 mM EDTA] and homogenized in a Dounce style homogenizer. Homogenates were centrifuged at 1000*g* (10 min at 4°C) to pellet nuclei and unbroken cells. The resulting post-nuclear homogenate (∼2.5 ml) was centrifuged for 1 h at 100 000*g* at 4°C, to yield a cytosolic (S100) fraction and a membrane pellet, which was resuspended in 1 ml of lysis buffer to yield the P100 membrane fraction. Protein concentration was determined for both fractions and these were resolved in SDS–PAGE gels (20 μg of protein per lane), and evaluated by immunoblotting.

Mice

All animal work was approved by and conformed to the standards of the Oregon Health & Science University Animal Care and Use Committee. *Mtmr13*$^{-/-}$ mice have been described previously (29). The majority of the mice analyzed here had been backcrossed for eight generations onto a C57BL/6 background. *Mtmr2*$^{-/-}$ mice contain a splice-accepting gene trap in intron 2–3 of *Mtmr2*, and will be described fully elsewhere.

Sciatic nerve morphology

Mice were perfused with EM fixative [1.5% glutaraldehyde, 1.5% PFA, 0.05 M sucrose, 0.25% $CaCl_2$, 0.1 M sodium cacodylate buffer (pH 7.4)]. Sciatic nerves were dissected and further fixed overnight. To examine myelin morphology in P3 mice, pups were euthanized and sciatic nerves were dissected and placed in EM fixative overnight. Toluidine blue semi-thin (1 μm) plastic cross-sections were prepared from the mid-sciatic nerve.

The entire transverse fascicular area (TFA) of the mid-sciatic nerve was imaged on an automated Olympus BX61 microscope with a motorized stage and OASIS controller. A 100× objective (U PLAN S-APO 100× oil, NA1.4) was used and images were acquired using a monochrome CCD F-View II camera controlled by the MicroSuite software (Ver 3.3). The montage feature in MicroSuite was used to capture the entire TFA without duplication. Fixed nerves (above) were processed for EM in a Lynx II automatic processor. Ultrathin (70 nm) sections were cut and contrasted further with uranyl acetate and lead citrate, and grids were viewed and photographed by using an FEI Tecnai 12 transmission electron microscope that is interfaced to an AMT XR16M CCD camera.

To determine the ratio of normal to abnormal fibers, the entire TFA was counted. Axons with an area of $\geq$15.8 μm^2 (axonal diameter of ~4.5 μm) were selected using image thresholding and the MetaMorph (Ver. 7.5.3.0) integrated morphometry analysis tool. Selected axons were counted and scored as normal or abnormal. An abnormal fiber was defined as one having an infolding, outfolding or deep invagination (approximately two-thirds of axon diameter or more). For P3 sciatic nerves, the size selection protocol (above) was not used. Instead, all myelinated axons were counted and scored as normal or abnormal. For P3 nerves, any axons that could not be clearly scored as normal or abnormal were scored as uncertain. These accounted for 0.5 to 1% of the fibers counted. To determine axon density, all visible myelinated fibers were counted in each 100× light image or 1200× EM image analyzed. The number of images analyzed was determined based on area, with 10% of total TFA being the target degree of coverage.

Images used for *g*-ratio determination were taken at 100× with identical light/camera settings. Image analysis was performed in MetaMorph. Only reasonably round fibers lacking infoldings or outfoldings were analyzed. For *Mtmr13*$^{-/-}$ nerves, every suitable axon in an image was measured. For wild-type animals, 10–15 of the rounder axons in each image were arbitrarily selected, with a goal of a roughly representative size distribution. Axons selected were generally between 2 and 11 μm in diameter and were not sectioned through Schmidt–Lanterman incisures. Axons were selected with the threshold tool (in MetaMorph), using the same threshold value for each image. At least 100 fibers per mouse were analyzed. Axon and myelin perimeters were measured using the integrated morphometry analysis tool. *G*-ratio was calculated by dividing the axon perimeter by the myelin perimeter. Effective axon diameter was calculated by dividing the axon perimeter by pi.

SUPPLEMENTARY MATERIAL

Supplementary Material is available at *HMG* online.

ACKNOWLEDGEMENTS

The authors wish to thank Gary Banker, Gary Westbrook, Jau-Shin Lou, Peter Mayinger and Sean Speese for helpful discussions and critical reading of the manuscript. Deconvolution microscopy and analysis were carried out in OHSU's Advanced Light Microscopy Core at The Jungers Center for Neurosciences Research. The authors wish to thank Aurelie Snyder and Stefanie Kaech Petrie of the Advanced Light Microscopy Core for expert advice. The authors wish to thank Robert Kayton, Lisa Dirling Vecchiarelli and Sue Aicher for assistance with electron microscopy, nerve preparation and expert advice. The 1D4B (LAMP-1) and E7 (β-tubulin) monoclonal antibodies, developed by Drs J. Thomas August and Michael Klymkowsky, respectively, were obtained from the Developmental Studies Hybridoma Bank developed under the auspices of the National Institutes of Health–National Institute of Child Health & Human Development and maintained by The University of Iowa, Department of Biology, Iowa City, IA 52242, USA.

Conflict of Interest statement. None declared.

FUNDING

This work was supported by the National Institutes of Health (NS057903 to F.L.R., NS061800 to Sue Aicher). The DeltaVison CoreDV microscope was purchased with a Shared Instrumentation Grant from the National Institutes of Health (RR023432 to Thomas Keller). The electron microscope was purchased through a grant from the Murdock Charitable Trust (to Sue Aicher).

REFERENCES

1. Di Paolo, G. and De Camilli, P. (2006) Phosphoinositides in cell regulation and membrane dynamics. *Nature*, **443**, 651–657.
2. Clague, M.J., Urbe, S. and de Lartigue, J. (2009) Phosphoinositides and the endocytic pathway. *Exp. Cell Res.*, **315**, 1627–1631.

3. Vanhaesebroeck, B., Guillermet-Guibert, J., Graupera, M. and Bilanges, B. (2010) The emerging mechanisms of isoform-specific PI3K signalling. *Nat. Rev. Mol. Cell Biol.*, **11**, 329–341.
4. McCrea, H.J. and De Camilli, P. (2009) Mutations in phosphoinositide metabolizing enzymes and human disease. *Physiology*, **24**, 8–16.
5. Skre, H. (1974) Genetic and clinical aspects of Charcot-Marie-Tooth's disease. *Clin. Genet.*, **6**, 98–118.
6. Scherer, S.S. and Wrabetz, L. (2008) Molecular mechanisms of inherited demyelinating neuropathies. *Glia*, **56**, 1578–1589.
7. Patzko, A. and Shy, M.E. (2011) Update on Charcot-Marie-Tooth disease. *Curr. Neurol. Neurosci. Rep.*, **11**, 78–88.
8. Pereira, J.A., Lebrun-Julien, F. and Suter, U. (2011) Molecular mechanisms regulating myelination in the peripheral nervous system. *Trends Neurosci.*, **35**, 123–134.
9. Previtali, S.C., Quattrini, A. and Bolino, A. (2007) Charcot-Marie-Tooth type 4B demyelinating neuropathy: deciphering the role of MTMR phosphatases. *Expert Rev. Mol. Med.*, **9**, 1–16.
10. Bolino, A., Muglia, M., Conforti, F.L., LeGuern, E., Salih, M.A.M., Georgiou, D.M., Christodoulou, K., Hausmanowa-Petrusewicz, I., Mandich, P., Schenone, A. *et al.* (2000) Charcot-Marie-Tooth type 4B is caused by mutations in the gene encoding myotubularin-related protein-2. *Nat. Genet.*, **25**, 17–19.
11. Senderek, J., Bergmann, C., Weber, S., Ketelsen, U.P., Schorle, H., Rudnik-Schoneborn, S., Buttner, R., Buchheim, E. and Zerres, K. (2003) Mutation of the SBF2 gene, encoding a novel member of the myotubularin family, in Charcot-Marie-Tooth neuropathy type 4B2/11p15. *Hum. Mol. Genet.*, **12**, 349–356.
12. Azzedine, H., Bolino, A., Taieb, T., Birouk, N., Di Duca, M., Bouhouche, A., Benamou, S., Mrabet, A., Hammadouche, T., Chkili, T. *et al.* (2003) Mutations in MTMR13, a new pseudophosphatase homologue of MTMR2 and Sbf1, in two families with an autosomal recessive demyelinating form of Charcot-Marie-Tooth disease associated with early-onset glaucoma. *Am. J. Hum. Genet.*, **72**, 1141–1153.
13. Hnia, K., Vaccari, I., Bolino, A. and Laporte, J. (2012) Myotubularin phosphoinositide phosphatases: cellular functions and disease pathophysiology. *Trends Mol. Med.*, **18**, 317–327.
14. Leslie, N.R., Davies, E.M., Sheffield, D.A., Tibarewal, P., Fedele, C.G. and Mitchell, C.A. (2012) The PTEN and myotubularin phosphoinositide 3-phosphatases: linking lipid signalling to human disease. *Subcell. Biochem.*, **58**, 281–336.
15. Zou, J., Majerus, P.W., Wilson, D.B., Schrade, A., Chang, S.C. and Wilson, M.P. (2011) The role of myotubularin-related phosphatases in the control of autophagy and programmed cell death. *Adv. Enzyme Regul.*, **52**, 282–289.
16. Robinson, F.L. and Dixon, J.E. (2006) Myotubularin phosphatases: policing 3-phosphoinositides. *Trends Cell Biol.*, **16**, 403–412.
17. Kim, S.A., Taylor, G.S., Torgersen, K.M. and Dixon, J.E. (2002) Myotubularin and MTMR2, phosphatidylinositol 3-phosphatases mutated in myotubular myopathy and type 4B Charcot-Marie-Tooth disease. *J. Biol. Chem.*, **277**, 4526–4531.
18. Berger, P., Bonneick, S., Willi, S., Wymann, M. and Suter, U. (2002) Loss of phosphatase activity in myotubularin-related protein 2 is associated with Charcot-Marie-Tooth disease type 4B1. *Hum. Mol. Genet.*, **11**, 1569–1579.
19. Schaletzky, J., Dove, S.K., Short, B., Lorenzo, O., Clague, M.J. and Barr, F.A. (2003) Phosphatidylinositol-5-phosphate activation and conserved substrate specificity of the myotubularin phosphatidylinositol 3-phosphatases. *Curr. Biol.*, **13**, 504–509.
20. Falasca, M. and Maffucci, T. (2009) Rethinking phosphatidylinositol 3-monophosphate. *Biochim. Biophys. Acta*, **1793**, 1795–1803.
21. Dove, S.K., Dong, K., Kobayashi, T., Williams, F.K. and Michell, R.H. (2009) Phosphatidylinositol 3,5-bisphosphate and Fab1p/PIKfyve under PPIn endo-lysosome function. *Biochem. J.*, **419**, 1–13.
22. Ho, C.Y., Alghamdi, T.A. and Botelho, R.J. (2012) Phosphatidylinositol-3,5-bisphosphate: no longer the poor PIP2. *Traffic*, **13**, 1–8.
23. Robinson, F.L. and Dixon, J.E. (2005) The phosphoinositide-3-phosphatase MTMR2 associates with MTMR13, a membrane-associated pseudophosphatase also mutated in type 4B Charcot-Marie-Tooth disease. *J. Biol. Chem.*, **280**, 31699–31707.
24. Berger, P., Berger, I., Schaffitzel, C., Tersar, K., Volkmer, B. and Suter, U. (2006) Multi-level regulation of myotubularin-related protein-2 phosphatase activity by myotubularin-related protein-13/set-binding factor-2. *Hum. Mol. Genet.*, **15**, 569–579.
25. Jean, S., Cox, S., Schmidt, E.J., Robinson, F.L. and Kiger, A.A. (2012) Sbf/MTMR13 coordinates PI(3)P and Rab21 regulation in endocytic control of cellular remodeling. *Mol. Biol. Cell*, **23**, 2723–2740.
26. Bolino, A., Bolis, A., Previtali, S.C., Dina, G., Bussini, S., Dati, G., Amadio, S., Del Carro, U., Mruk, D.D., Feltri, M.L. *et al.* (2004) Disruption of Mtmr2 produces CMT4B1-like neuropathy with myelin outfolding and impaired spermatogenesis. *J. Cell Biol.*, **167**, 711–721.
27. Bonneick, S., Boentert, M., Berger, P., Atanasoski, S., Mantei, N., Wessig, C., Toyka, K.V., Young, P. and Suter, U. (2005) An animal model for Charcot-Marie-Tooth disease type 4B1. *Hum. Mol. Genet.*, **14**, 3685–3695.
28. Tersar, K., Boentert, M., Berger, P., Bonneick, S., Wessig, C., Toyka, K.V., Young, P. and Suter, U. (2007) Mtmr13/Sbf2-deficient mice: an animal model for CMT4B2. *Hum. Mol. Genet.*, **16**, 2991–3001.
29. Robinson, F.L., Niesman, I.R., Beiswenger, K.K. and Dixon, J.E. (2008) Loss of the inactive myotubularin-related phosphatase Mtmr13 leads to a Charcot-Marie-Tooth 4B2-like peripheral neuropathy in mice. *Proc. Natl Acad. Sci. USA*, **105**, 4916–4921.
30. Bolis, A., Coviello, S., Bussini, S., Dina, G., Pardini, C., Previtali, S.C., Malaguti, M., Morana, P., Del Carro, U., Feltri, M.L. *et al.* (2005) Loss of Mtmr2 phosphatase in Schwann cells but not in motor neurons causes Charcot-Marie-Tooth type 4B1 neuropathy with myelin outfoldings. *J. Neurosci.*, **25**, 8567–8577.
31. Vaccari, I., Dina, G., Tronchere, H., Kaufman, E., Chicanne, G., Cerri, F., Wrabetz, L., Payrastre, B., Quattrini, A., Weisman, L.S. *et al.* (2011) Genetic interaction between MTMR2 and FIG4 phospholipid phosphatases involved in Charcot-Marie-Tooth neuropathies. *PLoS Genet.*, **7**, e1002319.
32. Bolis, A., Coviello, S., Visigalli, I., Taveggia, C., Bachi, A., Chishti, A.H., Hanada, T., Quattrini, A., Previtali, S.C., Biffi, A. *et al.* (2009) Dlg1, Sec8, and Mtmr2 regulate membrane homeostasis in Schwann cell myelination. *J. Neurosci.*, **29**, 8858–8870.
33. Ohnishi, A., Murai, Y., Ikeda, M., Fujita, T., Furuya, H. and Kuroiwa, Y. (1989) Autosomal recessive motor and sensory neuropathy with excessive myelin outfolding. *Muscle Nerve*, **12**, 568–575.
34. Gabreels-Festen, A.A., Joosten, E.M., Gabreels, F.J., Stegeman, D.F., Vos, A.J. and Busch, H.F. (1990) Congenital demyelinating motor and sensory neuropathy with focally folded myelin sheaths. *Brain*, **113**, 1629–1643.
35. Taveggia, C., Zanazzi, G., Petrylak, A., Yano, H., Rosenbluth, J., Einheber, S., Xu, X., Esper, R.M., Loeb, J.A., Shrager, P. *et al.* (2005) Neuregulin-1 type III determines the ensheathment fate of axons. *Neuron*, **47**, 681–694.
36. Michailov, G.V., Sereda, M.W., Brinkmann, B.G., Fischer, T.M., Haug, B., Birchmeier, C., Role, L., Lai, C., Schwab, M.H. and Nave, K.A. (2004) Axonal neuregulin-1 regulates myelin sheath thickness. *Science*, **304**, 700–703.
37. Flores, A.I., Narayanan, S.P., Morse, E.N., Shick, H.E., Yin, X., Kidd, G., Avila, R.L., Kirschner, D.A. and Macklin, W.B. (2008) Constitutively active Akt induces enhanced myelination in the CNS. *J. Neurosci.*, **28**, 7174–7183.
38. Goebbels, S., Oltrogge, J.H., Kemper, R., Heilmann, I., Bormuth, I., Wolfer, S., Wichert, S.P., Mobius, W., Liu, X., Lappe-Siefke, C. *et al.* (2010) Elevated phosphatidylinositol 3,4,5-trisphosphate in glia triggers cell-autonomous membrane wrapping and myelination. *J. Neurosci.*, **30**, 8953–8964.
39. Sherman, D.L., Krols, M., Wu, L.M., Grove, M., Nave, K.A., Gangloff, Y.G. and Brophy, P.J. (2012) Arrest of myelination and reduced axon growth when Schwann cells lack mTOR. *J. Neurosci.*, **32**, 1817–1825.
40. Razidlo, G.L., Katafiasz, D. and Taylor, G.S. (2011) Myotubularin regulates Akt-dependent survival signaling via phosphatidylinositol 3-phosphate. *J. Biol. Chem.*, **286**, 20005–20019.
41. MacKeigan, J.P., Murphy, L.O. and Blenis, J. (2005) Sensitized RNAi screen of human kinases and phosphatases identifies new regulators of apoptosis and chemoresistance. *Nat. Cell Biol.*, **7**, 591–600.
42. Chojnowski, A., Ravise, N., Bachelin, C., Depienne, C., Ruberg, M., Brugg, B., Laporte, J., Baron-Van Evercooren, A. and LeGuern, E. (2007) Silencing of the Charcot-Marie-Tooth associated MTMR2 gene decreases proliferation and enhances cell death in primary cultures of Schwann cells. *Neurobiol. Dis.*, **26**, 323–331.

43. Lee, O.K., Frese, K.K., James, J.S., Chadda, D., Chen, Z.H., Javier, R.T. and Cho, K.O. (2003) Discs-Large and Strabismus are functionally linked to plasma membrane formation. *Nat. Cell Biol.*, **5**, 987–993.
44. Gorczyca, D., Ashley, J., Speese, S., Gherbesi, N., Thomas, U., Gundelfinger, E., Gramates, L.S. and Budnik, V. (2007) Postsynaptic membrane addition depends on the Discs-Large-interacting t-SNARE Gtaxin. *J. Neurosci.*, **27**, 1033–1044.
45. Cotter, L., Ozcelik, M., Jacob, C., Pereira, J.A., Locher, V., Baumann, R., Relvas, J.B., Suter, U. and Tricaud, N. (2010) Dlg1-PTEN interaction regulates myelin thickness to prevent damaging peripheral nerve overmyelination. *Science*, **328**, 1415–1418.
46. Newbern, J.M., Li, X., Shoemaker, S.E., Zhou, J., Zhong, J., Wu, Y., Bonder, D., Hollenback, S., Coppola, G., Geschwind, D.H. *et al.* (2011) Specific functions for ERK/MAPK signaling during PNS development. *Neuron*, **69**, 91–105.
47. Ishii, A., Fyffe-Maricich, S.L., Furusho, M., Miller, R.H. and Bansal, R. (2012) ERK1/ERK2 MAPK signaling is required to increase myelin thickness independent of oligodendrocyte differentiation and initiation of myelination. *J. Neurosci.*, **32**, 8855–8864.
48. Lee, H.W., Kim, Y., Han, K., Kim, H. and Kim, E. (2010) The phosphoinositide 3-phosphatase MTMR2 interacts with PSD-95 and maintains excitatory synapses by modulating endosomal traffic. *J. Neurosci.*, **30**, 5508–5518.
49. Gary, J.D., Wurmser, A.E., Bonangelino, C.J., Weisman, L.S. and Emr, S.D. (1998) Fab1p is essential for PtdIns(3)P 5-kinase activity and the maintenance of vacuolar size and membrane homeostasis. *J. Cell Biol.*, **143**, 65–79.
50. Cooke, F.T., Dove, S.K., McEwen, R.K., Painter, G., Holmes, A.B., Hall, M.N., Michell, R.H. and Parker, P.J. (1998) The stress-activated phosphatidylinositol 3-phosphate 5-kinase Fab1p is essential for vacuole function in *S. cerevisiae*. *Curr. Biol.*, **8**, 1219–1222.
51. Johnson, E.E., Overmeyer, J.H., Gunning, W.T. and Maltese, W.A. (2006) Gene silencing reveals a specific function of hVps34 phosphatidylinositol 3-kinase in late versus early endosomes. *J. Cell Sci.*, **119**, 1219–1232.
52. Chow, C.Y., Zhang, Y., Dowling, J.J., Jin, N., Adamska, M., Shiga, K., Szigeti, K., Shy, M.E., Li, J., Zhang, X. *et al.* (2007) Mutation of FIG4 causes neurodegeneration in the pale tremor mouse and patients with CMT4J. *Nature*, **448**, 68–72.
53. Dang, H., Li, Z., Skolnik, E.Y. and Fares, H. (2004) Disease-related myotubularins function in endocytic traffic in *Caenorhabditis elegans*. *Mol. Biol. Cell*, **15**, 189–196.
54. Velichkova, M., Juan, J., Kadandale, P., Jean, S., Ribeiro, I., Raman, V., Stefan, C. and Kiger, A.A. (2010) *Drosophila* Mtm and class II PI3K coregulate a PI(3)P pool with cortical and endolysosomal functions. *J. Cell Biol.*, **190**, 407–425.
55. Parrish, W.R., Stefan, C.J. and Emr, S.D. (2004) Essential role for the myotubularin-related phosphatase Ymr1p and the synaptojanin-like phosphatases Sjl2p and Sjl3p in regulation of PI(3)P in yeast. *Mol. Biol. Cell*, **15**, 3567–3579.
56. Arighi, C.N., Hartnell, L.M., Aguilar, R.C., Haft, C.R. and Bonifacino, J.S. (2004) Role of the mammalian retromer in sorting of the cation-independent mannose 6-phosphate receptor. *J. Cell Biol.*, **165**, 123–133.
57. Krajewski, K.M., Lewis, R.A., Fuerst, D.R., Turansky, C., Hinderer, S.R., Garbern, J., Kamholz, J. and Shy, M.E. (2000) Neurological dysfunction and axonal degeneration in Charcot-Marie-Tooth disease type 1A. *Brain*, **123**, 1516–1527.
58. Goebbels, S., Oltrogge, J.H., Wolfer, S., Wieser, G.L., Nientiedt, T., Pieper, A., Ruhwedel, T., Groszer, M., Sereda, M.W. and Nave, K.A. (2012) Genetic disruption of Pten in a novel mouse model of tomaculous neuropathy. *EMBO Mol. Med.*, **4**, 486–499.
59. Nave, K.A. (2010) Myelination and support of axonal integrity by glia. *Nature*, **468**, 244–252.
60. Berger, P., Tersar, K., Ballmer-Hofer, K. and Suter, U. (2011) The CMT4B disease-causing proteins MTMR2 and MTMR13/SBF2 regulate AKT signalling. *J. Cell. Mol. Med.*, **15**, 307–315.
61. Gillooly, D.J., Morrow, I.C., Lindsay, M., Gould, R., Bryant, N.J., Gaullier, J.M., Parton, R.G. and Stenmark, H. (2000) Localization of phosphatidylinositol 3-phosphate in yeast and mammalian cells. *EMBO J.*, **19**, 4577–4588.
62. Ikonomov, O.C., Sbrissa, D. and Shisheva, A. (2001) Mammalian cell morphology and endocytic membrane homeostasis require enzymatically active phosphoinositide 5-kinase PIKfyve. *J. Biol. Chem.*, **276**, 26141–26147.
63. Rutherford, A.C., Traer, C., Wassmer, T., Pattni, K., Bujny, M.V., Carlton, J.G., Stenmark, H. and Cullen, P.J. (2006) The mammalian phosphatidylinositol 3-phosphate 5-kinase (PIKfyve) regulates endosome-to-TGN retrograde transport. *J. Cell Sci.*, **119**, 3944–3957.
64. Lorenzo, O., Urbe, S. and Clague, M.J. (2006) Systematic analysis of myotubularins: heteromeric interactions, subcellular localisation and endosome related functions. *J. Cell Sci.*, **119**, 2953–2959.
65. Previtali, S.C., Zerega, B., Sherman, D.L., Brophy, P.J., Dina, G., King, R.H., Salih, M.M., Feltri, L., Quattrini, A., Ravazzolo, R. *et al.* (2003) Myotubularin-related 2 protein phosphatase and neurofilament light chain protein, both mutated in CMT neuropathies, interact in peripheral nerve. *Hum. Mol. Genet.*, **12**, 1713–1723.
66. Goryunov, D., Nightingale, A., Bornfleth, L., Leung, C. and Liem, R.K. (2008) Multiple disease-linked myotubularin mutations cause NFL assembly defects in cultured cells and disrupt myotubularin dimerization. *J. Neurochem.*, **104**, 1536–1552.
67. Franklin, N.E., Taylor, G.S. and Vacratsis, P.O. (2011) Endosomal targeting of the phosphoinositide 3-phosphatase MTMR2 is regulated by an N-terminal phosphorylation site. *J. Biol. Chem.*, **286**, 15841–15853.
68. Yoshimura, S., Gerondopoulos, A., Linford, A., Rigden, D.J. and Barr, F.A. (2010) Family-wide characterization of the DENN domain Rab GDP-GTP exchange factors. *J. Cell Biol.*, **191**, 367–381.
69. Ratner, N., Williams, J.P., Kordich, J.J. and Kim, H.A. (2006) Schwann cell preparation from single mouse embryos: analyses of neurofibromin function in Schwann cells. *Methods Enzymol.*, **407**, 22–33.